View metadata, citation and similar papers at core.ac.uk

brought to you by CORE

provided by DSpace at VU

This is a postprint of

Wind-induced resuspension in a shallow lake from Medium Resolution Imaging Spectrometer (MERIS) full-resolution reflectances

Eleveld, M.A.

Water Resources Research, 48(4), n/a

Published version: http://dx.doi.org/10.1029/2011WR011121

Link VU-DARE: http://hdl.handle.net/1871/38053

(Article begins on next page)

Wind-induced resuspension in a shallow lake from Medium Resolution Imaging Spectrometer (MERIS) full-resolution reflectances

Marieke A. Eleveld

Vrije Universiteit Amsterdam, Institute for Environmental Studies (VU-IVM),
De Boelelaan 1087, 1081 HV Amsterdam, the Netherlands
E-mail: marieke.eleveld@ivm.vu.nl; T 31 20 5989591; F 31 20 5989553

Abstract

A lack of empirical evidence impedes assessment of the spatial and temporal extent of critical conditions for recurring high turbidity in large wind-exposed shallow lakes. Here spatio-temporal variation in total suspended matter (TSM) concentration was captured by processing 30 Envisat Medium Resolution Imaging Spectrometer (MERIS) images of a shallow lake (Markermeer) with a spectral matching algorithm. The TSM maps showed elevated downwind concentrations for moderate winds (from 4 to 9 m s^{-1}), which occur 68 % of the time. Regressions confirmed the relationship between hourly averaged wind speed and TSM. To explore critical conditions for resuspension, wind speed, linear fetch, and water depth were combined in a spatial model based on simplified linear wave equations. Remotely sensed TSM patterns matched predicted areas of resuspension from these wave equations. On average, over 70% of cells were true positive or negative, with elevated TSM matching the predicted resuspending bottom area, and background TSM matching no resuspension. Images acquired during moderate winds register local resuspension. This implies that under these conditions, a critical shear stress threshold for resuspension is passed, followed by upward mixing over the few meters of water column. Images acquired during low wind speeds ($\leq$ 3 m s^{-1}) either do not show a TSM pattern, or display settling, because it takes several hours of low wind before all particles are removed from the visible top layer. Because of the good spatial matching, the resuspension model can also be used for future verification of the retrieval capacity of the spectral matching algorithm.

An edited version of this paper was published by AGU. Copyright (2012) American Geophysical Union.

Please go to http://dx.doi.org/10.1029/2011WR011121 if your library has a **subscription** to **Water Resources Research**, or to view the published **open** abstract.

Always cite as: Eleveld, M. A. (2012), Wind-induced resuspension in a shallow lake from Medium Resolution Imaging Spectrometer (MERIS) full-resolution reflectances, *Water Resour. Res., 48*(4), W04508, doi:10.1029/2011WR011121.

1. Introduction

Resuspension of sediments by wave action can greatly affect water quality of shallow lakes, because it (temporary) increases turbidity and enhances nutrient cycling by bringing sedimentary nutrients back into the water column [*Kristensen et al.*, 1992; *Søndergaard et al.*,1992; *De Vicente et al.*, 2006]. Resuspended sediments can easily reach the surface layers, because shallow lakes are permanently mixed (polymictic) forming a large turbulently mixed top layer. Particles are lifted from bed to water column when the water movement at the sediment-water interface is strong enough to pass the critical shear stress [*Luettich et al.*, 1990].

Resuspension of bottom sediments in shallow lakes with little horizontal flow has been modeled through the semi-empirical Sverdrup-Munk-Bretschneider relationship with wind-induced wave action [*Carper and Bachmann*, 1984; *Gons et al.*, 1986]. Wind blowing over a certain fetch length and for a particular water depth will induce orbital velocity at the bottom, and if a critical (shear stress) threshold is passed, sediment is mixed up to the surface layers, where its optical signal may be detected by remote sensing [*Miller et al.*, 2005]. Subsequently, such a signal can be used to derive the near-surface mass concentration of total suspended matter (TSM). Are the predicted critical thresholds related to these surface concentrations? One way to extend Carper and Bachman's resuspension analysis to considering actual surface concentrations would be to incorporate the opposite vertical sediment transport flux. This downward flux can be calculated as a (measured or estimated) settling speed times concentration [*Somlyódy*, 1982; *Aalderink et al.*, 1984; *Blom et al.*, 1994]. Alternatively, three-dimensional Computational Fluid Dynamics (CFD) modeling for water flow under wind-induced mixing can be used to estimate transport from the convection-diffusion equation. Subsequently, the predicted spatial variability in concentrations has been compared with concentrations from remote sensing [*Hedger et al.*, 2002 for chlorophyll; *Van Kessel et al.*, 2009 and *Van der Wal et al.*, 2010 for TSM).

In this article, TSM concentrations are predicted from their optical characteristics using remote measurements of electromagnetic radiation that generate synoptic observations of shallow lakes. For these waters with several optically active components, empirical concentration retrieval algorithms introduce inaccuracies for many wavelengths in the optical range [*Pavelsky and Smith*, 2009; *Tarrant et al.*, 2010]. Therefore, the spectral signatures, absorption and scattering of the primary in-water physical parameters were used to derive concentrations from reflectance [*Dekker et al.*, 2002; *Vos et al.*, 2003; *Eleveld et al.*, 2008]. These retrievals of the concentrations of water quality parameters are now enabled by a numerical solution of the radiative transfer (RT) model [*Mobley and Sundman*, 2001] and subsequent application of spectral matching algorithms [*Mobley et al.*, 2005; *Smyth et al.*, 2006: *Hommersom et al.*, 2010]. Measured remote sensing reflectances were matched with modeled remote sensing reflectances. Modeled reflectances come with underlying solar and in-water absorption and scattering parameters [*Van der Woerd and Pasterkamp*, 2008]. Application of such an algorithm to a shallow lake is novel and exciting, because absorbing and scattering substances accumulate in these enclosed water bodies. The quality of the remote sensing spectra is however dependent on aerosol retrieval and atmospheric correction over these lakes [*Giardino et al.*, 2007]. Can the resuspension models perhaps also be used to verify results from ocean color algorithms?

This paper addresses TSM patterns in a recurrently turbid inland water body, a shallow wind-exposed lake called Markermeer (Lake Marken or Lake Markermeer). It aims to bring together remote sensing and a spatial implementation of a generic resuspension model to explore

critical conditions (water depth, fetch length, wind speed) for resuspension in a shallow lake. The paper first discusses the use of reflectance measurements from the satellite sensor for matching with the results from the radiative transfer model, which was calibrated with the lake's specific absorption and scattering properties. Subsequently, resulting TSM concentrations were interpreted using co-occurring wind conditions. Then, a model was setup for the four main unidirectional wind conditions for speeds 1 to 10 m s^{-1} and combined with bathymetry to derive areas of likely resuspension. Results have been compared to elucidate critical conditions influencing the TSM concentrations, and to verify the retrieval capacity of the HYDROPT algorithm [*Van der Woerd and Pasterkamp*, 2008].

2. Study area

The Markermeer is a 680 km^2 large, fresh water lake with an average depth of 3.6 m (Figure 1). A maximum fetch of 33.6 km can be reached. Occasional diurnal stratification is easily broken down by wind and wave action. The wind climate for Markermeer (the Netherlands) is influenced by mid-latitude westerlies and depressions following the Gulf Stream in the direction of Norway. Associated gradients in air pressure and fronts cause temporary southerly and easterly winds followed by the prevailing southwesterlies. Local wind strength and direction are also influenced by land and sea breezes because of differential heating between land and water surfaces. Wind data are available for Schiphol (Figure 1) from KNMI (http://www.knmi.nl/samenw/hydra/cgi-bin/meta_data.cgi).

Sixty percent of the flat bottom of Markermeer is covered with a fine silty layer, known as IJsselmeer deposits [*Van Duin*, 1992]. On top of this layer resides a benthic fluffy layer consisting of easily resuspended organic material [*Vijverberg et al.*, 2011]. The area was part of an inland sea, which was closed by dam in 1932. Since 1976, the lake has been separated from the IJsselmeer (Lake IJssel) by the Houtribdijk (Houtrib dike), a remnant from an abandoned polder reclamation. Nowadays, water levels in the lake are regulated to about -0.2 m above sea level in summer to facilitate drainage to agricultural land, and when possible to -0.4 m in winter to facilitate run off of surplus water, and residence time of the water is 1.2 years. No major rivers drain directly into Markermeer, and import of TSM through the sluices was considered negligible [*Van Duin*, 1992; *Vijverberg et al.*, 2011].

The internal TSM source of the lake consists of wind-induced resuspension of bottom sediments. Average transparency is 0.30 to 0.50 m, average chlorophyll concentrations range from 40 to 60 mg m^{-3}, macrophytes cover 5 % of the lake bottom [*Mooij et al.*, 2005]. In situ data on several water quality parameters are available for Rijkswaterstaat stations (Figure 1). Currently, measures are being sought to overcome high turbidity. It is thought that high TSM concentrations affect the zebra mussels (*Dreissena*) by clogging their gills, and that the associated light attenuation impedes the growth of water plants, whereas algae and (toxic) cyanobacteria thrive at higher TSM concentrations [*Van Duin*, 1992; *Scheffer*, 1998].

SEE FIG. 1

3. Retrieval of TSM from remote sensing reflectance

3.1. Selection of MERIS data

Ocean color sensors measure radiance with the high spectral and radiometric sensitivity required for differentiation of substances in the water. Additionally, high spatial resolution is usually required for lake monitoring. The MEdium Resolution Imaging Spectrometer (MERIS) instrument on board ESA's ENVISAT spacecraft delivers imagery with a full (about 300 x 300 m^2) and reduced (about 1 x 1 km^2) spatial resolution. Thirty full resolution (FR) images that were cloud free over most of the research area were selected from the EOLI-SA catalogue (http://earth.esa.int/EOLi/EOLi.html). The obtained Level 2 (L2) data were already processed up to water-leaving reflectance with standard ESA atmospheric correction, MEGS 7.4 / IPF 5.05 [*Moore and Aiken*, 2000]:

$$\rho_w^{0+}(\theta_v,\phi) = \frac{\pi L_u^{0+}(\theta_v,\phi)}{E_d^{0+}} = \pi\rho_{rs} \quad (1)$$

Above water-leaving reflectance (ρ_w^{0+}) equals half a hemisphere (π) of water-leaving radiances (L_u^{0+}) over the downward incident irradiance above the water surface (E_d^{0+}) (see Table 1 for notation). The angles θ_v and ϕ are the sensor viewing zenith angle and the differential azimuth between sun and sensor.

SEE TABLE 1

The definition of remote sensing reflectance (ρ_{rs}) in equation 1 also implies that the contribution of electromagnetic radiance from the substances in the atmosphere (such as aerosols) have been removed from the total signal registered by the satellite sensor, but the standard ESA atmospheric correction [*Moore et al.*, 1999; *Moore and Aiken*, 2000] is under investigation. High backscatter and absorption in both atmosphere (by aerosols from land such as dust and soot) and water (by extreme concentrations of optically active substances) can confuse the atmospheric correction software [*Guanter et al.*, 2010], which can result in selection of an erroneous aerosol model [*Moore et al.*, 1999; *Zagolski et al.*, 2007]. This misinterpretation of aerosol type causes underestimation of reflectance in the shorter wavelengths of the L2 data, where signals are already low because of high absorption by chlorophyll-*a* (CHL), TSM and colored dissolved organic matter (CDOM).

Specifically for lakes, it has been attempted to revert to (not atmospherically corrected) Level 1b top of atmosphere (TOA) radiance data to correct for stray light from nearby vegetated land [*Vidot and Santer*, 2005] and make a customized atmospheric correction using VISAT/BEAM Java plug-ins [*Hommersom et al.*, 2010; *Brockmann Consult*, 2011]. Because of its specific Inherent Optical Properties, this was less successful for Markermeer (see also *Binding et al.*, 2011 for Lake of the Woods).

Instead, the 30 MERIS Full Resolution L2 images for 2006 were processed using HYDROPT [*Van der Woerd and Pasterkamp*, 2008], which uses band differences in its χ^2 fitting of measured and modeled reflectances to make it less sensitive to remaining biases from the applied aerosol model. Band 1 comprising reflectance at detector averaged center wavelength of

413 nm (bandwidth 10 nm) was excluded from the processing because of occasional occurrence of negative reflectances in this band [*Zibordi et al.*, 2006; *Zagolski et al.*, 2007] due to overcorrection for atmospheric effects. All water pixels were processed: the suite of additional MERIS product confidence flags was only used for a-posteriori quality checking. This approach successfully compensates for some problems in atmospheric correction, which made careful use of the L2 data feasible [*Van der Wal et al.*, 2010].

3.2. Optical modeling

In theory, the water-leaving reflectances (ρ_w^{0+}) at wavelength (λ) from the L2 data sets can be related to the inherent optical properties (IOPs) total absorption coefficient (a in m^{-1}) and total backscatter coefficient (b_b in m^{-1}) through a factor f':

$$\rho_w^{0+}(\lambda) = \frac{\pi f' \Re}{Q} \frac{b_b}{a + b_b} \tag{2}$$

This f' factor varies with sun zenith angle and with IOPs [*Morel and Gentilli*, 1991]. $\Re$ represents reflection and refraction effects at the air-sea interface [*Morel and Gentilli*, 1996]. Q relates upwelling radiance to upwelling irradiance just beneath the air-sea interface [*Ruddick et al.*, 2006].

Specific inherent optical properties (sIOPs) relate absorption and scattering to concentrations of individual optically active substances. sIOPs are defined as normalized absorption (a^*) or scattering (b^*) per unit concentration of mass, m^2 (mg CHL)$^{-1}$ or m^2 (g TSM)$^{-1}$ respectively, and for CDOM absorption normalized at 440 nm. For the eight Markermeer sIOP sets of June 1999 [*Pasterkamp*, 2001], water samples had been filtered to measure first TSM, and after extraction in ethanol, chlorophyll-*a* (and phaeopigment) concentrations. Radiance had been measured on site with a PR-650 field-spectroradiometer (Photo Research, Chatsworth, CA, USA). Spectra of absorption (a) and beam attenuation (c) had been measured using a Philips PU8800 UV/VIS double-beam lab-spectrophotometer. The TSM (seston) absorption spectrum was derived from the measured optical density on the filter. The absorption spectrum of tripton (the inorganic part of TSM) on the filter was obtained after bleaching of the pigments from the filter using hot ethanol. The phytoplankton absorption spectrum was derived by subtracting the tripton spectrum from the TSM spectrum. The absorption of the dissolved humic substances (CDOM) in the filtrate and the beam attenuation of the water sample were determined from optical density measurements in a cuvette. The scattering coefficient (b) was estimated by subtraction of the absorption coefficients from the beam attenuation coefficient [*Rijkeboer et al.*, 1998].

The resulting mean specific absorption and scattering coefficients of Markermeer are given in Table 2. Careful study of these otherwise robust results reveals an absorption signal in a^*_{TSM} at 665 nm that could indicate a problem with TSM bleaching. In this paper, TSM is broadly defined as indicating *total* suspended matter, which is usually present in the form of flocs, small clay particles bound with organic material into delicate aggregates that can also contain fine silt [*Van Duin*, 1992; *Vijverberg et al.*, 2011].

SEE TABLE 2

Actual *implementation* in HYDROPT is based on a lookup table (LUT) describing the relationship of remote sensing reflectances (ρ_{rs}) with a range of inherent optical properties and other environmental conditions as calculated by the forward radiative transfer model Hydrolight [*Mobley and Sundman*, 2001]. To populate the LUT, Hydrolight was parameterized with the properties of three independent components: 1 pure water characterized by the pure-water absorption, scattering and phase function; 2 absorption (alias chlorophyll in Hydrolight) with user defined total absorption; 3 particle scattering (alias minerals) with total scattering assuming the Petzold average particle phase function. Other Hydrolight settings were: an idealized sky model and uniform background sky, no bioluminescence, no fluorescence or Raman scattering, a wind speed of 5 m s^{-1}, and an optically infinitely deep water column (for these turbid waters). Thus the LUT stored modeled reflectances (ρ_{rs}) at MERIS band centers (modeled spectra) for every possible combination of a physically realistic set of IOPs (total a and b) and angles (solar zenith angle θ_0, vertical nadir angle θ_v and azimuth angle ϕ).

The inversion comprises a spectral matching algorithm – the HYDROPT algorithm searches the modeled spectrum that best matches a spectrum for each measured pixel [*Van der Woerd and Pasterkamp*, 2008]. This was implemented as a χ^2 merit function based on the squared difference in remote sensing reflectance in the consecutive bands (equation 3).

$$\chi^2 = \sum_{i=1}^{N-1}\left[\frac{\Delta\rho_{rs,i} - \Delta\rho_{rs}\left(\lambda_i, C_m, \theta_0, \theta_v, \phi\right)}{\sigma_i}\right]^2 \tag{3}$$

$\Delta\rho_{rs,i}$ is the difference in observed remote sensing reflectance between consecutive bands. $\Delta\rho_{rs}(\lambda_i, C_m, \theta_0, \theta_v, \phi)$ is the difference in modeled remote sensing reflectance between consecutive bands (for wavelength interval λ_i, a set of modeled concentrations C_m, and modeled viewing and solar geometries θ_0, θ_v, and ϕ). σ_i is the estimated uncertainty in $\Delta\rho_{rs,i}$. N is the number of spectral bands for the fit.

As previously explained, the LUT contains the link to the total IOPs; the decomposition into concentrations (C) of single substance optical components (k) was realized as follows:

$$\frac{\partial a}{\partial C_k} = \left(1-\alpha_k\right) a_k^*\left(C_k\right)^{-\alpha_k} \;,\; \frac{\partial b}{\partial C_k} = (1-\beta_k) b_k^*(C_k)^{-\beta_k} \tag{4}$$

Presuming that both α and β equal 1, results in the linear sIOP definition:

$$a_k^* = \frac{a_k}{C_k} \text{ and } b_k^* = \frac{b_k}{C_k} \tag{4a}$$

To complete the inversion, the derivatives of the natural logarithmic value of the remote sensing reflectance $\partial\ln(\rho_{rs})$ and the derivatives of the concentrations (C_k) were expressed as a function of natural logarithms of total a and b, $x_1 = \ln(a)$ and $x_2 = \ln(b)$:

$$\frac{\partial \ln(\rho_{rs})}{\partial C_k} = \frac{\partial \ln(\rho_{rs})}{\partial x_1}\frac{\partial x_1}{\partial C_k} + \frac{\partial \ln(\rho_{rs})}{\partial x_2}\frac{\partial x_2}{\partial C_k} \tag{5}$$

Thus, the inverse model estimates the concentrations of, amongst others TSM from MERIS water-leaving radiance reflectance data at 6 optical wavelength intervals (Table 2). Subsequently, the retrieved TSM data were compared against independent in situ measurements.

3.3. In situ TSM data for inter-comparison

Independent gravimetric in situ measurements of TSM (sampling depth 1 m below water surface) were obtained from the Rijkswaterstaat monitoring stations that were visited several (9-12) times per year (Figure 1). These in situ concentrations, and HYDROPT TSM concentrations from the Full Resolution (FR) images were plotted for "Markermeer midden" (MM), the station furthest (about 10 km) from the shore (and therefore least influenced by radiation from land). True match-ups of remote sensing and in situ samples during unclouded conditions at overpass are rare [*Eleveld et al.*, 2008]. Comparison of the two datasets was performed when the time difference was two days maximally, which should be perceived as verification rather than as formal validation [*Mélin et al.*, 2007]. To increase material for comparison, additional MERIS Reduced Resolution (RR) data were processed to TSM concentrations when they matched in situ monitoring data plus or minus one day difference. For RR images matching the FR images, TSM_{RR} and $TSMF_{FR}$ are highly correlated ($TSM_{RR} = 0.98 TSM_{FR} + 1.69$; $r^2 = 0.95$, $F = 477.30$, n = 27, $p << 0.0001$).

4. Modeling of resuspension

4.1. Wind data

To investigate how surface TSM is related to wind speed, hourly averaged data were downloaded for the Schiphol station from KNMI (http://www.knmi.nl/samenw/hydra/cgi-bin/meta_data.cgi). These data were plotted next to the retrieved TSM maps and correlated with retrieved TSM. The sampling of TSM by remote sensing is synoptic and instantaneous, but biased for cloud free conditions.

4.2. Spatial modeling

The wind data were also used to analyze how surface TSM is related to wind energy, speed and direction, and whether wind-induced wave orbitals would reach the bottom boundary layer and induce resuspension and upward mixing of bottom sediment.

First, the north oriented bathymetric data (Figure 1) were regridded to 300 m × 300 m cells – corresponding with MERIS-FR resolution, so that the main data sources have the same cell size – and used to make a land-water map. The distance the wind travels over open water as straight-line fetch [*USACE*, 2002] for the 4 main wind directions was determined by counting, for each cell, the number of water cells with an upwind water cell. It was assumed here that the wind speed at Schiphol was valid over the entire water surface, although corrections to overwater wind for large fetch have also been discussed [*Bishop et al.*, 1992; *USACE*, 2002].

Subsequently, simulations with the Sverdrup-Munk-Bretschneider relationship for deep water waves (equation 6; *Carper and Bachmann*, 1984) were made to estimate the wave periods (T in s) from these four straight line fetches (F) for wind speeds (u) ranging from 1 to 10 m s^{-1} (with steps of 1 m s^{-1}).

$$\frac{gT}{2\pi u} = 1.20 \tanh\left[0.077\left(\frac{gF}{u^2}\right)^{0.25}\right] \quad (6)$$

Deep water wave growth formulae can be applied to shallow water conditions with the constraint that no wave period can grow past a limiting value. The predicted wave period (T) was compared to the shallow-water limit (T_p) given in equation 7. d is water depth in m, g is gravity. Wave periods were not greater than this limiting T_p value and the deepwater values were retained.

$$T_p = 9.78 \cdot \left(\frac{d}{g}\right)^{\frac{1}{2}} \quad (7)$$

The wave period was subsequently used to calculate wavelength (L in m) using equation 8.

$$L = \frac{g \cdot T^2}{2\pi} \quad (8)$$

Then, the maximum depth at which a water wave's passage causes significant water motion (the wave base) was calculated by taking half the wavelength [*Carper and Bachmann*, 1984]. One half is chosen because for that value the tanh- term in linear wave theory equations (equation 9) approaches one and deep water waves become transitional waves [*USACE*, 2002].

$$L = \frac{gT^2}{2\pi} \tanh\left(\frac{2\pi d}{L}\right) = \frac{gT}{\omega} \tanh(kd) \quad (9)$$

k = wave number, ω = angular frequency

Resuspension occurs when deep water waves enter water shallower than the wave base. The differences between wave base and water depth (d) indicate where resuspension of the lake bottom is possible for the selected wind conditions (equation 6). If the difference is large, much of the wave energy reaches the bottom. If bed composition is relatively homogenous, as for Markermeer, it is an indicator of resuspension intensity (Miller et al., 2005). Particle size itself is no variable in this resuspension model.

Also, to get some insight into the current estimate of wave conditions, the equation for wave growth with fetch (equation 10, derived from the JONSWAP growth law of peak frequency [*USACE*, 2002]) was used to calculate the time of wind duration ($t_{F,u}$ in min.) needed to achieve steady state conditions:

$$t_{F,u} = 77.23 \cdot \frac{F^{0.67}}{u^{0.34} \cdot g^{0.33}} \quad (10)$$

where t in this equation is the wind duration (in min). This appeared to take from ($t_{1\ km,\ 10\ m/s}$) 16 mins to ($t_{30\ km,\ 1\ m/s}$) almost 6 hours. Stable wind conditions do frequently occur for such a time

span, because of autocorrelation in the wind time series (see Discussion). Therefore, the waves can indeed steadily grow with fetch. Thus, the conditions for applying the simplified wave predictions (equations 6 and 8) are met.

A distinction of the dominant mechanism, resuspension versus other (such as advection or settling) was derived from matching these theoretical resuspension maps for wind conditions during acquisition with the TSM maps from remote sensing [*Foody*, 2002].

5. Results

5.1. Multi-temporal retrieved and in situ TSM

Multi-temporal TSM values extracted at Markermeer midden (FR) are in line with regular in situ monitoring data (Figure 2a). Similarities are striking for the match-ups on either the same day or with a difference of two days from in situ measurements, on 3 May, 29 June, 26 July (two match-ups), 20 Sept. (two match-ups), 16 Oct., and 15 Nov. 2006 (Figure 2c). These match-ups are all in the lower TSM range. Additional RR data (RR) did not contain the 15 Nov. match-up, but it provided an interesting extra RR match-up of 35.4 g m^{-3} for 10 Dec. when wind speed was 4.1 m s^{-1}. This RR match-up corresponded with the high in situ TSM value of 140 g m^{-3} on 11 Dec. when wind speeds had steadily increased to hourly average of 11.3 and occasionally 12 m s^{-1}(Figure 2b). This latter match-up was left out of the regression (Figure 2c), but when included the trend line obviously deviates considerably from 1:1 and the relation is not significant ($TSM_{RR} = 0.09TSM_{in\ situ} + 24.2$; $r^2 = 0.16$, $F = 1.11$, $n = 8$, $p < 0.34$). Without the outlier, both correlations between $TSM_{in\ situ}$ and TSM_{FR} and $TSM_{in\ situ}$ and TSM_{RR} in Figure 2c have high coefficients of determination and are significant ($r^2 = 0.87$, $p < 0.0008$ and $r^2 = 0.71$, $p < 0.02$, respectively, see Figure 2c). For further verification of the HYDROPT output for Markermeer, results from additional highly significant correlations with in situ *turbidity* measurements were added as Supplementary material[1].

SEE FIG. 2

5.2. Retrieved spatial TSM patterns

Figure 3 shows three TSM concentration maps, which were derived from the MERIS-FR remote sensing reflectance data. High downwind concentrations (> 50 g m^{-3}) were observed in the northeast against de Houtribdijk after westerly winds (Figure 3a). Upwind concentrations along the western (Noord-Holland) lakeshore and in the IJmeer (station PP, Figure 1) are about three times lower. Hourly mean wind speed at acquisition on 17 April 2006 was 7.2 m s^{-1} from westerly direction (280°). Mean wind speed over the 24 hours prior to acquisition was 4.8 m s^{-1} and wind directions were predominantly westerly to south-westerly.

Figures. 3b and c show maps of subsequent days with short-term decreasing wind speeds (at acquisition). They show a clear directional TSM signal followed by lower concentration caused by net settling when the wind abated. The image of 10 May 2006 (Figure 3b) shows highest concentrations in the southwestern part of Markermeer, which were delineated by a deep

[1] Auxiliary materials are available in the HTML. doi:10.1029/2011WR011121. (AND AT THE END OF THIS FILE)

navigation channel in the southeast (see Figure 1). High concentrations likely result because fetch is long enough to enable resuspension or horizontal advection. Instantaneous wind was 5.5 m s^{-1} from the northeast; average wind velocity over the last 24 hours was 5.3 m s^{-1}. On 11 May (4c) concentrations at the center of the lake dropped to almost half the concentrations in Figure 3b, but they were still relatively high near the western lake shore and navigation channel. Instantaneous wind speed had dropped to 2.1 m s^{-1}, and average wind speed was 3.2 m s^{-1}. Over the whole period, the wind showed an abating trend and winds were veering from northeast to east before becoming variable. Quiet conditions, low wind and subsequent wave action caused surface concentrations to drop: the settling flux is higher than resuspension.

In summary, main differences between the TSM maps are due to differences in conditions at acquisition. Mean hourly wind speed seems to match well with the residence times of TSM in the visible layer. High TSM conditions at downwind locations concur with moderate wind speeds at acquisition on 17 April and 10 May. Moderate wind speeds could cause resuspension at and advection to the downwind side of the lake. Low concentrations concur with low wind speed at acquisition on 11 May. Settling might explain low TSM concentrations when both wind speed at acquisition and mean wind speed over the last hours are consistently lower.

SEE FIG. 3

5.3. Empirical relations between retrieved TSM and wind speed

A significant relationship was found between lake averaged retrieved TSM concentrations and wind speed, u (r^2 = 0.40, F = 19.02, n = 30, p < 0.0002, Figure 4). The coefficient of determination is slightly higher for TSM against u^2, (TSM = $0.59u^2$ + 17.00; r^2 = 0.48, F = 25.40, n = 30, p < 0.00003). Higher correlation was expected because u^2 scales proportional to bottom shear stress [*Luettich et al.*, 1990]. The plots also suggest a background TSM signal followed by a sharp increase that describes the unsaturated part of the empirical sigmoidal function between TSM and wind speed in a resuspension-settling balance model [*Scheffer*, 1998]. In the present study such a model gives TSM = $19.64 + 0.13u^{2.74}$; r^2 = 0.49, F = 40.13, n = 30, p << 0.00001.

SEE FIG. 4

5.4. Simulated resuspension by the wave model

The most likely two causes for highest concentrations in downwind directions at a given wind speed (Figures 3a and b) are that minimum fetch length for resuspension was exceeded here, or that upwind resuspension occurred earlier and TSM at the surface accumulates by downwind advection. Figure 5 shows prediction maps of lakebed area prone to resuspension for the hourly averaged wind conditions that match with acquisition time of Figure 3. Colored areas in Figure 5a roughly correspond to areas of high concentration in Figure 3a (17 April), which indicates that local resuspension is an important source for surface TSM. Minor differences in orientation between the area of highest resuspension intensity and the patch of highest concentrations reflect the difference between modeled unidirectional westerly wind and the real, more variable wind field, which was south-westerly three hours before acquisition. Striping, or shifts in plotted resuspension intensity is a model artifact that reflects the impact of protrusions

of the land-water boundary (such as headlands or a peninsula) on linear fetch, the distance wind travels over open water. Table 3 gives modeled resuspension for the in situ stations, and shows, for western winds (as in Figure 5a), that fetch is just over 20 km for station LH, which has a local water depth of 4.27 m and is located in the eastern part of the lake. Therefore, estimated wind velocities required to initiate local sediment resuspension are at least 5 m s^{-1} – a theoretical critical wind speed value that corresponds to the observations from the remote sensing products (Figure 3a). For the centrally located station MM, the critical wind speed for resuspension is 6 m s^{-1}; BH and HH fall just outside the area were resuspension was predicted to occur (Figure 5a).

Figure 5b complements Figure 3b, the first (10 May) map from a pair with decreasing wind speed in subsequent days (24 h difference). There are some differences between 3b and 5b. High concentrations in Figure 3b are delineated by the navigation channel, whereas this channel has only a local effect in 5b (the cells still have an upwind water cell, but the wave base doesn't reach the channel bed). Differences can also be explained by the wind being NE (40°) instead of simulated full N. The latter also amplified the impact of shelter from the Marken peninsula (east of station MG) on fetch and hence on resuspension.

These examples illustrate that, for wind speeds of 4 m s^{-1} and higher, patterns in TSM concentrations and predicted resuspension (intensity) match to some extent, despite simplifications in comparison and linear fetch modeling. After all, these are based on instantaneous hourly averaged wind speed for main directions. The maps match well when elevated TSM matches with predicted resuspension (true positive) and when background TSM matches with no resuspension (true negative). Indeed, a cell-wise comparison of Figures 3a (17 April) and 5a, and Figures 3b (10 May) and 5b shows that when thresholds for elevated TSM were varied from background, about 20 g m^{-3}, to observed highs, about 50 g m^{-3}, true positive and true negative together account for 56 – 80 % of cells (on 17 April) and 62 - 69 % of cells (on 10 May), respectively.

Net settling explains low TSM concentrations when both wind speed at acquisition and mean wind speed are consistently lower. For wind speeds of 3 m s^{-1} and lower, patterns are virtually absent (not presented) or remaining patterns seem inherited and reflect slow settling (as illustrated by Figure 3c). For the latter case (Figure 3c), acquisition had been preceded by 7 hrs of wind speed < 3 m s^{-1} and 13 hrs of wind speed < 4 m s^{-1}. The TSM patterns have no link with instantaneous resuspension, which affects less than 0.4 % of lake bottom (Figure 6), because a 2 m s^{-1} wind speed cannot generate sufficient mixing for water movement at the sediment-water interface to pass the critical shear stress threshold for resuspension. Actually, results from a sensitivity analysis of the spatial modeling (Figure 6) are that less than 2.5 % of the entire lake bottom sediment surface area can be disturbed by wave activity at wind velocities up to 3 m s^{-1} from any direction. Wind speeds ≥ 4 m s^{-1} seem to indicate that resuspension fluxes become predominant; resuspension fluxes are higher than settling fluxes for 2.7 – 13.4 % of the total lake surface. At 6 m s^{-1} over half the lake bottom area (60 %) supplies material for resuspension. More than 84 % can be disturbed by wave activity at wind velocities ≥ 10 m s^{-1} from any direction.

SEE FIG. 5, TABLE 3 AND FIG. 6

6. Discussion

6.1. Mechanisms, timescales and extrapolation over the water column

The remote sensing results give a spatial overview of horizontal variation in TSM concentrations. For wind speeds ≤ 3 m s^{-1}, patterns are virtually absent (not presented) in the TSM maps, or could reflect slow *settling* of at least some of the TSM fractions as illustrated by Figure 3c. Material with a net settling speed (w) of 0.4 m day^{-1} [*Van Duin*, 1992; *Vlag*, 1992; *Van Kessel et al.*, 2009] has a residence time of one day in the top layer of the water column observed by the satellite, (Figures 3b and 3c). However, resuspension can also entrain a coarser fraction, which settles more quickly, 2 m day^{-1} [*Van Kessel et al.*, 2009] or even faster [*Van Duin*, 1992; *Vlag*, 1992]. Settling is also a *local*, vertical transport mechanism: during settling, the wind has not enough energy to drive strong advection currents. Finally, there is also a background TSM concentration (Figure 4) consisting of riverine and atmospheric input, and (suspended) phytoplankton and cyanobacteria influenced by the interacting biological and physical and biological processes such as production and decomposition [*Van Duin*, 1992].

The results of this study also support the general notion that resuspension and its surface expression can be nearly instantaneous in shallow lakes due to the short distance to the surface (Figures 3a and b). The model predicts the local resuspension (not advection) for hourly averaged wind conditions matching satellite data acquisition time. Good spatial matching of retrieved TSM with results from the model suggests that high surface TSM during moderate winds of 4 to 9 m s^{-1} is mainly from *local resuspension*. Patterns match for concurrent hourly averaged wind conditions. Water depth is on average 3.6 m. A net upward resuspension rate of 3.6 m per hour (0.001 m s^{-1}) is plausible. Advection, over much larger distances (e.g. 6 km) would require currents of over 1.67 m s^{-1}. These simply do not occur. This is also supported by *Luettich et al.* [1990] and *Chung et al*. [2009], who found that the bottom shear stresses associated with the horizontal currents are generally too small to influence TSM concentrations. Bottom shear is proportional to the velocity gradient in the boundary layer. Since the maximum bottom orbital velocity at Markermeer varies between 0.0 and 0.5 m s^{-1} over a small boundary layer, and the mean current velocity for advective flow varies between 0.0 and 0.2 m s^{-1} over a boundary layer that encompasses the entire water column [*Van Duin*, 1992], it seems reasonable to focus on wave-stress as forcing responsible for eroding bottom sediments, and to use wave equations for local resuspension modeling.

These processes and their timescales were ignored when performing simple linear regressions of concentrations from remote sensing on hourly averaged wind speed at acquisition (Figure 4). Nevertheless, the regressions perform well. Possibly, autocorrelation in the wind speed time-series could also partly explain this. Wind speeds are autocorrelated up to 151 h (over 6 days), with the strongest correlation ($r > 0.4$) within 12 h. Significant correlations between lake averaged retrieved TSM and wind speed ($p < 0.05$) occur for time lags ranging from 0 - 48 hours before, but only up to four hours after acquisition. Because resuspension varies substantially with wind speed (equation 6), resuspension modeling also performs well. Note that even for the relatively fast resuspension processes, well-developed waves with defined direction, and relatively long wavelengths are required (equation 10).

The remote sensing data did not sample during *strong winds* (Figure 4), which distinguished this study from investigations of sudden temporal variations of suspended solid concentrations during passing of a front or storm [*Cózar et al.*, 2005; *Miller et al.*, 2005]. During

strong winds over Markermeer, remotely sensed surface TSM will probably not provide a good representation of horizontal and vertical concentrations over the entire water column. Although *Luettich et al.* [1990] found that a two-layer vertical structure of horizontal circulation is unlikely to form during resuspension events in shallow lakes, recent measurements in Markermeer show that strong bottom currents can occur under high winds (> 10 m s^{-1}), both as bottom return flows from wave setup [*Van Kessel et al.*, 2009] and from density differences due to formation of fluid mud [*Vijverberg et al.*, 2011]. Waves induce this liquefaction of the cohesive sediment bed, and maintain the unconsolidated state of this mud below the lutocline [*Bachman et al.*, 2005]. A 3D model (see Introduction) is a good alternative for predicting TSM concentrations for these high wind conditions, or for extrapolating remotely sensed surface TSM concentrations over profiles with steep concentration gradients to the bottom should remote sensing data for these windy (and often cloudy) conditions be available.

6.2. Methodological implications and outlook from inter-comparison of results

The use of MERIS L2 data, HYDROPT with a linear sIOP model, and calibration with a mean local sIOP set resulted in TSM maps that complied with in situ TSM data (Figure 2) and correlated well with wind speed (Figure 4). Patterns in TSM from remote sensing (Figure 3) match maps from the simple resuspension model based on wind speed, direction and bathymetry (Figure 5). For Markermeer a typical threshold for resuspension (u_{crit}) is 4 m s^{-1}, with most resuspension at the shallow downwind areas in the west and north (Figure 1) under easterly and southerly winds (Figure 6). Similar predictions from resuspension models have been compared to in situ measurements in the past. They generally confirmed local occurrence of sediment resuspension events when wind velocities exceeded depth-dependent critical velocities [*Carper and Bachmann*, 1984; *Kristensen et al.*, 1992; *Douglas and Rippey*, 2000]. However, *Gons et al.* [1986] could not establish a clear threshold for resuspension for Loosdrechtse Plassen (Lake Loosdrecht), which they mainly attributed to the location of the validation stations. Yet after the pioneering work by *Sheng and Lick* [1979], resuspension models have hardly been subjected to a truly spatial evaluation, as presented here. Model results might deviate from remote sensing results in case of direct supply of large quantities of TSM by rivers [*Giardino et al.*, 2010]. Finally, local complexities in other lakes might also call for a more advanced third generation wave model such as SWAN [*Booij et al.*, 1999].

Careful checking of occasional divergence between TSM from remote sensing and resupension predictions also provides – perhaps unexpected – additional information. When the differences cannot be attributed to variable wind conditions or any other apparent conditions or processes that were not captured in the resuspension model, they can also be used to check if problems with the atmospheric correction of the L2 data remain (see Section 3.1). Such an approach is portable to other shallow lakes, if their bathymetry, bottom characteristics, wind conditions, are known [*Lehner and Döll*, 2004]. When remote sensing data with optimal atmospheric correction become available, and new optical in situ measurements are made, HYDROPT also enables simultaneous mapping of both the material properties of resuspended TSM, and further optical characterization of (organic) background concentrations [*O'Donnell et al.*, 2010]. Then the method, a spectral matching algorithm [*Mobley et al.*, 2005; *Hommersom et al.*, 2010; *Van der Wal et al.*, 2010] which can easily be parameterized with local lake sIOPs is ideal, also for application in other lakes.

Acknowledgments.
The MERIS data used in this study were provided by the European Space Agency (ESA), through Category 1 project 4168, the in situ data were provided by Rijkswaterstaat, Ministry of Infrastructure and the Environment (Directie IJsselmeergebied). Further support was provided by a grant from the Netherlands Agency for Aerospace Programmes (NIVR) GO project code 53601RW. Reinold Pasterkamp is thanked for the HYDROPT software library. Jan Vermaat (VU), Daphne van der Wal (NIOZ) and three anonymous reviewers are thanked for comments on the manuscript.

References

Aalderink, R. H., L. Lijklema, J. Breukelman, W. van Raaphorst and A. G. Brinkman (1984), Quantification of wind induced resuspension in a shallow lake, *Water Sci. & Technol., 17*(6-7), 903–914.

Bachmann, R. W., M. V. Hoyer, S. B. Vinzon and D. E. Canfield, Jr. (2005), The origin of the fluid mud layer in Lake Apopka, Florida, *Limnol. Oceanogr.*, *50*(2), 2005, 629-635, doi:10.4319/lo.2005.50.2.0629.

Blom, G., E. H. S. van Duin and J. E. Vermaat (1994), Factors contributing to light attenuation in Lake Veluwe, Chapter 10, in *Lake Veluwe, a macrophyte-dominated system under eutrophication stress, Geobotany 21*, edited by W. Van Vierssen, M Hootsmans and J. Vermaat, pp. 158–174, Kluwer, Dordrecht (NL), ISBN 0–7923–2320–3.

Binding, C. E., T. A. Greenberg, J. H. Jerome, R. P. Bukata and G. Letourneau (2011), An assessment of MERIS algal products during an intense bloom in Lake Woods, *J. Plankton Res., 33*(5), 793-806, doi:10.1093/plankt/fbq133

Bishop, C. T., M. A. Donelan and K. K. Kahma (1992), Shore protection manual's wave prediction reviewed, *Coastal Engineering, 17*, 25-48, doi:10.1016/0378-3839(92)90012-J.

Booij, N., R. C. Ris, L. and H. Holthuijsen (1999) A third-generation wave model for coastal regions 1:Model description and validation. J. Geophys. Res., 104(C4): 7649–7666, doi:10.1029/98JC02622.

Brockmann Consult, (2011), ESA BEAM wiki. http://www.brockmann-consult.de/beam-wiki/ (Accessed 20 June 2011).

Carper, G. L. and R. W. Bachmann (1984), Wind resuspension of sediments in a prairie lake, *Canadian J. of Fisheries and Aquat. Sci., 41*, 1763–1767, doi:10.1139/f84-217.

Chung, E. G., F. A. Bombardelli and G. Schladow (2009), Sediment resuspension in a shallow lake, *Water Resources Res., 45*, W05422, doi:10.1029/2007WR006585.

Cózar, A., J. A. Gálvez, V. Hull, C. M. García and S. A. Loiselle (2005), Sediment resuspension by wind in a shallow lake of Esteros del Iberá (Argentina): a model based on turbidimetry, *Ecol. Modell., 186*(1), 63–76, doi:10.1016/j.ecolmodel.2005.01.020.

De Vicente, I., V. Amores and L. Cruz-Pizarro (2006), Instability of shallow lakes: A matter of the complexity of factors involved in sediment and water interaction? *Limnetica, 25*(1-2), 253–270. ISSN: 0213-8409.

Dekker, A. G., R. J. Vos and S. W. M. Peters (2002), Analytical algorithms for lake water TSM estimation for retrospective analyses of TM and SPOT sensor data, *Int. J. Remote Sens., 23*(1), 15–35, doi: 10.1080/01431160010006917.

Douglas, R. W. and B. Rippey (2000), The random redistribution of sediment by wind in a lake, *Limnol. Oceanogr., 45*(3), 686–694, doi:10.4319/lo.2000.45.3.0686.

Eleveld, M. A., R. Pasterkamp, H. J. van der Woerd and J. D. Pietrzak (2008), Remotely sensed seasonality in the spatial distribution of sea-surface suspended particulate matter in the southern North Sea, *Estuarine Coastal and Shelf Sci., 80*(1), 103–113, doi:10.1016/j.ecss.2008.07.015.

Foody, G. M. (2002), Status of land cover classification accuracy assessment, *Remote Sens. Environ., 80*(1), 185–201, doi:10.1016/S0034-4257(01)00295-4.

Giardino, C., V. E. Brando, A. G. Dekker, N. Strömbeck and G. Candiani (2007), Assessment of water quality in Lake Garda (Italy) using Hyperion, *Remote Sens. Environ., 109*(2), 183–195, doi:10.1016/j.rse.2006.12.017.

Giardino C., M. Bresciani, P. Villa and A. Martinelli (2010), Application of remote sensing in water resource management: the case study of Lake Trasimeno, Italy, *Water Resour. Manage., 24*, 3885-3899, doi:10.1007/s11269-010-9639-3.

Gons, H. J., R. Veeningen, R and Van Keulen (1986), Effects of wind on a shallow lake ecosystem: resuspension of particles in the Loosdrecht Lakes, *Hydrobiological Bull., 20*(1/2), 109–120, doi:10.1007/BF02291156.

Guanter, L., A. Ruiz-Verdú, D. Odermatt, C. Giardino, S. Simis, V. Estellés, T. Heege, J. A. Domínguez-Gómez and J. Moreno (2010), Atmospheric correction of ENVISAT/MERIS data over inland waters: Validation for European lakes, *Remote Sens. Environ., 114*(3), 467–480, doi:10.1016/j.rse.2009.10.004.

Hedger, R. D., N. R. B. Olsen, T. J. Malthus and P. M. Atkinson (2002), Coupling remote sensing with computational fluid dynamics modelling to estimate lake chlorophyll-a concentration, *Remote Sens. Environ., 79*(1), 111–122, doi:10.1016/S0034-4257(01)00244-9.

Hommersom, A., S. Peters, H. J. van der Woerd, M.A. Eleveld, J. de Boer (2010), Chi-square spectral fitting for concentration retrieval, automatic local calibration, quality control, and water type detection, *Can. J. Remote Sens., 36*(6), 650–670. doi:10.5589/m11-004

Kristensen, P., M. Søndergaard and E. Jeppesen (1992), Resuspension in a shallow eutrophic lake, *Hydrobiologia, 228*(1), 101–109, doi:10.1007/BF00006481.

Lehner, B. and P. Döll (2004), Development and validation of a global database of lakes, reservoirs and wetlands, *J. Hydrology, 296*(1-4), 1-22, doi:10.1016/j.jhydrol.2004.03.028.

Luettich, R. A., Jr., D. R. F. Harleman and L. Somlyody (1990), Dynamic Behavior of Suspended Sediment Concentrations in a Shallow Lake Perturbed by Episodic Wind Events, *Limnol. Oceanogr., 35*(5), 1050-1067, doi:10.4319/lo.1990.35.5.1050.

Mélin, F., G. Zibordi, and J.-F. Berthon (2007), Assessment of satellite ocean color products at a coastal site. *Remote Sens. Environ., 110*(2), 192-215, 2007, doi:10.1016/j.rse.2007.02.026

Miller, R. L., B. A. McKee and E.J. d'Sa (2005), Monitoring bottom sediment resuspension and suspended sediments in shallow coastal waters, in *Remote sensing of coastal aquatic environments,* edited by R. J. Miller, C. E. del Castillo, B. A. McKee, pp. 259–276, Springer, Dordrecht (NL), ISBN: 1-4020-3099-1.

Mobley, C. D. and L. K. Sundman, (2001), *Hydrolight 4.2: Users' guide*. (Sec. printing, Oct. 2001), Sequoia Scientific, Redmond (WA, USA), 88 pp. http://www.sequoiasci.com/products/Hydrolight.aspx (Accessed 20 June 2011).

Mobley C. D., L. K. Sundman, C. O. Davis, J. H. Bowles, T.V. Downes, R. Leathers, M. J. Montes, W. P. Bissett, D. D. R. Kohler, R. P. Reid, E. M. Louchard, and A. Gleason (2005), Interpretation of hyperspectral remote-sensing imagery via spectrum matching and look-up tables, *Applied Optics, 44*(17), 3576–3592, doi:10.1364/AO.44.003576.

Mooij, W. M., S. Hülsmann, L.N. de Senerpont Domis, B.A. Nolet, P.L.E. Bodelier, P.C.M. Boers, L.M. Dionisio Pires, H. J. Gons, B. W. Ibelings, R. Noordhuis, R. Portielje, K. Wolfstein and E. H. R. R. Lammens (2005), The impact of climate change on lakes in the Netherlands: a review, *Aquat. Ecol., 39*(4), 381–400, doi:10.1007/s10452-005-9008-0.

Moore, G. F. and J. Aiken (2000), Case 2 (S) bright pixel atmospheric correction, *Algorithm Theoretical Basis Document ATBD 2.6*, Issue 4. Revision 1. Plymouth Marine Laboratory, Plymouth, UK. http://envisat.esa.int/instruments/meris/atbd/ (Accessed 20 June 2011).

Moore, G. F., J. Aiken and S. J. Lavender (1999), The atmospheric correction of water colour and the quantitative retrieval of suspended particulate matter in Case II waters: application to MERIS, *Int. J. Remote Sens., 20*(9), 1713–1733, doi:10.1080/014311699212434.

Morel, A. and B. Gentili (1991), Diffuse reflectance of oceanic waters: its dependence on sun angle as influenced by molecular scattering contribution, *Applied Optics, 30*(3), 4427–4438, doi:10.1364/AO.30.004427.

Morel, A. and B. Gentili (1996), Diffuse reflectance of oceanic waters. III. Implications of bidirectionality for the remote sensing problem, *Applied Optics* 35(24), 4850–4862, doi:10.1364/AO.35.004850.

Pasterkamp, R., (2001), Overzicht optische bibliotheek van Nederlandse watertypes. Meetcampagnes uitgevoerd door het IVM van 1995 t/m 2001, *VU-IVM report W01-23*, Vrije Universiteit, Amsterdam (NL).

O'Donnell, D. M., S. W. Effler, C. M. Strait and G. A. Leshkevich (2010), Optical characterizations and pursuit of optical closure for the western basin of Lake Erie through in situ measurements. *J. Great Lakes Res., 36*(4), 736–746, doi:10.1016/j.jglr.2010.08.009.

Pavelski, T. M. and L. C. Smith (2009), Remote sensing of suspended sediment concentration, flow velocity, and lake recharge in the Paece-Athabasca Delta, Canada, *Water Resources Res., 45*, W 11417, doi:10.1029/2008WR007424.

Rijkeboer, M., A. G. Dekker and H. J. Gons (1998), Subsurface irradiance reflectance spectra of inlands waters differing in morphology and hydrology, *Aquat. Ecol., 31*(3), 313–323, doi: 10.1023/A:1009916501492.

Ruddick, K. G., V. De Cauwer, Y.-J. Park and G. Moore (2006), Seaborne measurements of near infrared water-leaving reflectance: The similarity spectrum for turbid waters, *Limnol. Oceanogr., 51*(2), 1167–1179, doi:10.4319/lo.2006.51.2.1167.

Scheffer, M. (1998), *Ecology of shallow lakes*, Chapman & Hall, London (UK), 357 pp, ISBN 0-412-74920-3.

Sheng, Y. P. and W. Lick (1979), The transport and resuspension of sediments in a shallow lake, *J. Geophys. Res., 84*(C4), 1809–1826, doi:10.1029/JC084iC04p01809.

Smyth, T. J., G. F. Moore, T. Hirata and J. Aiken (2006), Semianalytical model for the derivation of ocean color inherent optical properties: description, implementation, and performance assessment, *Applied Optics, 45*(31), 8116–8131, doi:10.1364/AO.45.008116.

Somlyódy, L., (1982), Water-quality modelling: a comparison of transport-oriented and ecology-oriented approaches, *Ecol. Modell., 17*(3-4), 183–207, doi:10.1016/0304-3800(82)90031-X.

Søndergaard, M., P. Kristensen and E. Jeppesen (1992), Phosphorous release from resuspended sediment in shallow and wind-exposed Lake Arresø, Denmark, *Hydrobiologia, 228*(1), 91–99, doi:10.1007/BF00006480.

Tarrant, P. E., J.A. Amacher and S. Neuer (2010), Assessing the potential of Medium-Resolution Imaging Spectrometer (MERIS) and Moderate-Resolution Imaging Spectroradiometer (MODIS) data for monitoring total suspended matter in small and intermediate sized lakes and reservoirs, *Water Resources Res., 46*, W 09532, doi:10.1029/2009WR008709.

USACE (U.S. Army Corps of Engineers) (2002), *Coastal Engineering Manual (CEM)*. Engineer Manual 1110-2-1100, U.S. Army Corps of Engineers, Washington, D.C. (in 6 volumes). http://chl.erdc.usace.army.mil/ (Accessed 20 June 2011).

Van Duin E. H. S. (1992), Sediment transport, light and algal growth in the Markermeer. A two-dimensional water quality model for a shallow lake. PhD-thesis Landbouwuniversiteit Wageningen, Wageningen (NL).

Van der Wal D., T. van Kessel, M. A. Eleveld and J. Vanlede (2010), Spatial heterogeneity in estuarine mud dynamics, *Ocean Dynamics, 60*(3), 519–533, doi:10.1007/s10236-010-0271-9.

Van der Woerd, H. J. and R. Pasterkamp (2008), HYDROPT: A fast and flexible method to retrieve chlorophyll-a from multispectral satellite observations of optically complex coastal waters, *Remote Sens. Environ., 112*(4), 1795–1807, doi 10.1016/j.rse.2007.09.001.

Van Kessel, T, G. de Boer, and P. Boderie, P. (2009), Calibration suspended sediment model. Markermeer, *Report Q4612*, Deltares, Delft, the Netherlands.

Vidot, J. and R. Santer (2005), Atmospheric correction for inland waters application to SeaWIFS, *Int. J. Remote Sens., 26*(17), 3663–3682, doi:10.1080/01431160500034029.

Vijverberg, T., J. C. Winterwerp, S. G. J. Aarninkhof and H. Drost (2011), Fine sediment dynamics in a shallow lake and implication for design of hydraulic Works. *Ocean Dynamics, 61*(2-3), 187-202, doi 10.1007/s10236-010-0322-2.

Vlag, D. P. (1992), A model for predicting waves and suspended silt concentration in a shallow lake. *Hydrobiologia, 235/236*, 119–131, doi:10.1007/BF00026205.

Vos, R. J., J. H. M. Hakvoort, R. W. J. Jordans and B. W. Ibelings (2003), Multiplatform optical monitoring of eutrophication in temporally and spatially variable lakes. *Sci. Total Environ., 312*, 221–243, doi:10.1016/S0048-9697(03)00225-0.

Zagolski, F., R. Santer and O. Aznay (2007), A new climatology for atmospheric correction based on aerosol inherent optical properties, *J. Geophys. Res.-Atmospheres, 112*, D14208, doi:10.1029/2006JD007496.

Zibordi, G., F. Mélin and J.-F. Berthon (2006), Comparison of SeaWiFS, MODIS and MERIS radiometric products at a coastal site, *Geophys. Res. Lett., 33*, L06617, doi:10.1029/2006GL025778.

Table 1. Notation and nomenclature for optical parameters and implementation in the optical model[a]

Symbol	Name, units
a , a_k	total absorption, absorption for one of the individual optical components CHL, TSM, CDOM, m^{-1}.
a_k^*	specific absorption coefficients for any of the single optical components, for CHL m^2 mg^{-1}, for TSM m^2 g^{-1}, for CDOM m^{-1}.
b , b_k	total scattering, scattering for one of the individual the optical components, m^{-1}.
b_k^*	specific scattering coefficients for any of the single optical components, for TSM m^2 g^{-1}.
b_b	total backscattering, m^{-1}
C_k , C_m	concentration of a single optical substance (for CHL, mg m^{-3}; for TSM, g m^{-3}; for CDOM absorption, normalized by CDOM absorption at 440 nm). *m* distinguishes modeled concentrations.
E_d^{0+}	downwelling incident irradiance on a horizontal plane above the water surface, W m^{-2} nm^{-1}.
f'	a reflectance model factor, -.
i	counts intervals between consecutive bands, -.
k	a single optical substance such as chlorophyll (CHL), total suspended matter (TSM) or colored dissolved organic matter (CDOM), -.
$L_u^{0+}(\theta_v,\phi)$	water-leaving radiance (the upwelling radiance measured above the water surface in the sensor viewing direction), W m^{-2} nm^{-1} sr^{-1}.
N	number of spectral band used in the fit, -.
Q	a factor that relates radiance below the water surface to irradiance below the water surface, -.
x_1, x_2	natural logarithms of total a and total b, m^{-1}.
α_k	wavelength dependent exponential term in the specific absorption model, -.
β_k	wavelength dependent exponential term in the specific scattering model, -.
θ_0	solar zenith angle, deg.
θ_v	sensor view zenith angle, deg.
λ	wavelength of light, nm.
ρ_{rs}	remote sensing reflectance (sr^{-1}).
$\Delta\rho_{rs,i}$	difference in remote sensing reflectance in consecutive bands (sr^{-1}).
ρ_w^{0+}	water-leaving reflectance from a plane above the water surface, MERIS reflectance.
σ_i	estimated uncertainty in $\Delta\rho_{rs,i}$, -.
ϕ	relative sensor-sun azimuth angle, deg.

[a]For brevity spectral (λ) and angular factors (θ,ϕ) are usually left out. CHL, chlorophyll; TSM, total suspended matter, CDOM, colored dissolved organic matter.

Table 2. For wavelengths corresponding to the MERIS bands, the absorption and scattering (in m^{-1}) of pure water, the absorption per unit concentration for chlorophyll-a (m^2 mg^{-1}), absorption and scattering per unit concentration for suspended particular matter (m^2 g^{-1}), and absorption (m^{-1})[a] of colored dissolved organic matter. Scattering of CHL (and CDOM) were assumed zero. (Source: Pasterkamp, 2001)

Wavelength	**Absorption**				**Scattering**	
	Pure water	CHL	TSM	CDOM	Pure water	TSM
413[b]	0.0046	0.0167	0.0630	1.5846	0.0047	0.4754
442	0.0068	0.0183	0.0507	0.9816	0.0035	0.4629
490	0.0150	0.0140	0.0305	0.5134	0.0023	0.4458
510	0.0325	0.0086	0.0231	0.4115	0.0019	0.4423
560	0.0619	0.0030	0.0139	0.2541	0.0013	0.4208
620	0.2755	0.0048	0.0108	0.1528	0.0009	0.3787
665	0.4290	0.0068	0.0145	0.1157	0.0006	0.3459
681[b]	0.4696	0.0125	0.0102	0.1012	0.0006	0.3387
708	0.7040	0.0005	0.0036	0.0786	0.0005	0.3369

[a]Normalized at 440 nm.
[b]Band 1 (center wavelength 413 nm) and 8 (681 nm) were not used because of their sensitivity to atmospheric correction and possible contribution of fluorescence to the reflectance signal, respectively.

Table 3. Fetch for the four main wind directions ($F_{N,\ E,\ S,\ W)}$ and critical wind speeds (u_{crit}) for the onset of resuspension for the in situ stations BH to MM[a]

Station	BH	LH	PP	MG	HH	MM
depth (m)	2.89	4.27	2.99	2.39	2.23	4.24
location	N	E	S	W	W	Center
F_N (m) | u_{crit} (m/s)	1800 | 9	17700 | 6	30600 | 4	20400 | 4	2400 | 9	13800 | 6
F_E (m) | u_{crit} (m/s)	6000 | 6	3300 | 10	3000 | 7	1200 | 9	25200 | 4	14100 | 6
F_S (m) | u_{crit} (m/s)	25500 | 4	2100 | >10	3300 | 7	13500 | 4	9300 | 5	11700 | 6
F_W (m) | u_{crit} (m/s)	2400 | 9	20100 | 5	7200 | 5	2400 | 7	3000 | 9	10800 | 6

[a]See Figure 1. BH, Broekerhaven; LH, Lelystad-haven; PP, Pampus oost; MG, Marken Gouwzee; HH, Hoornse Hop; MM, Markermeer midden.

Figures

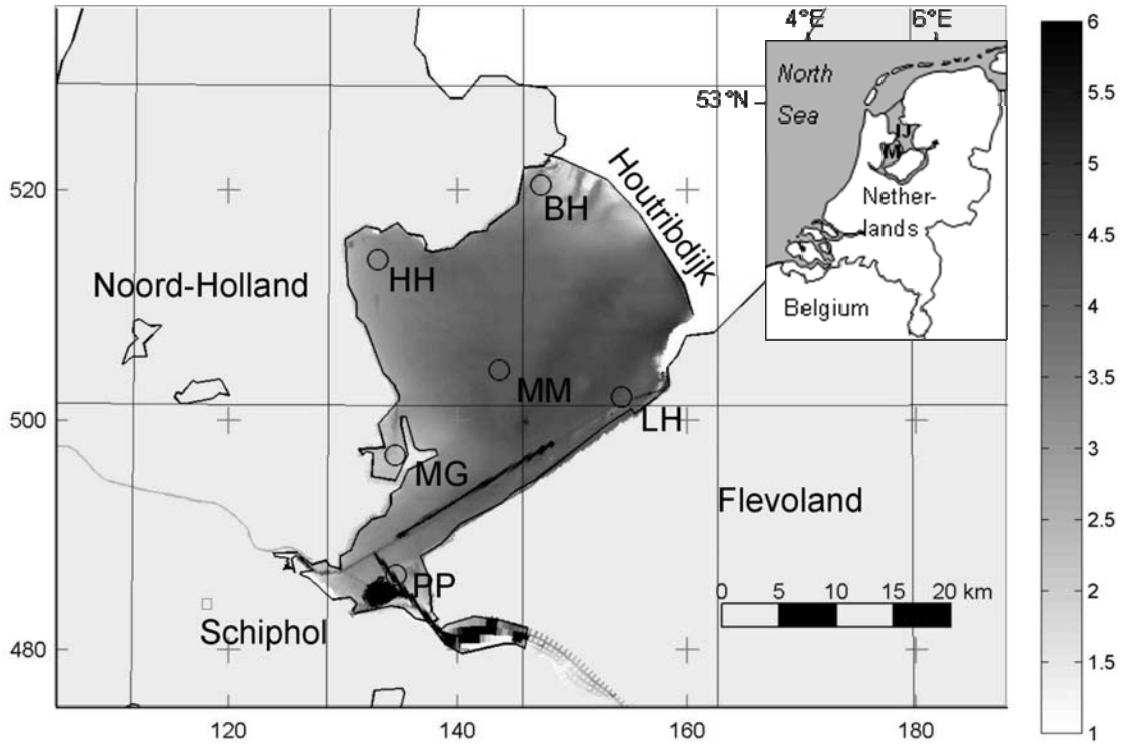

Figure 1. Water depth (in m) in Markermeer. Location of Rijkswaterstaat in situ water quality monitoring stations Broekerhaven (BH), Lelystad-haven (LH), Pampus oost (PP), Marken Gouwzee (MG), (Hoornse Hop (HH), no measurements), and Markermeer midden (MM). Location of KNMI weather station Schiphol. Coordinates are in km (Dutch RD system). (Inset) Location of the research area in the Netherlands (M indicates Markermeer, IJ indicates IJsselmeer) with geographical coordinates in degrees.

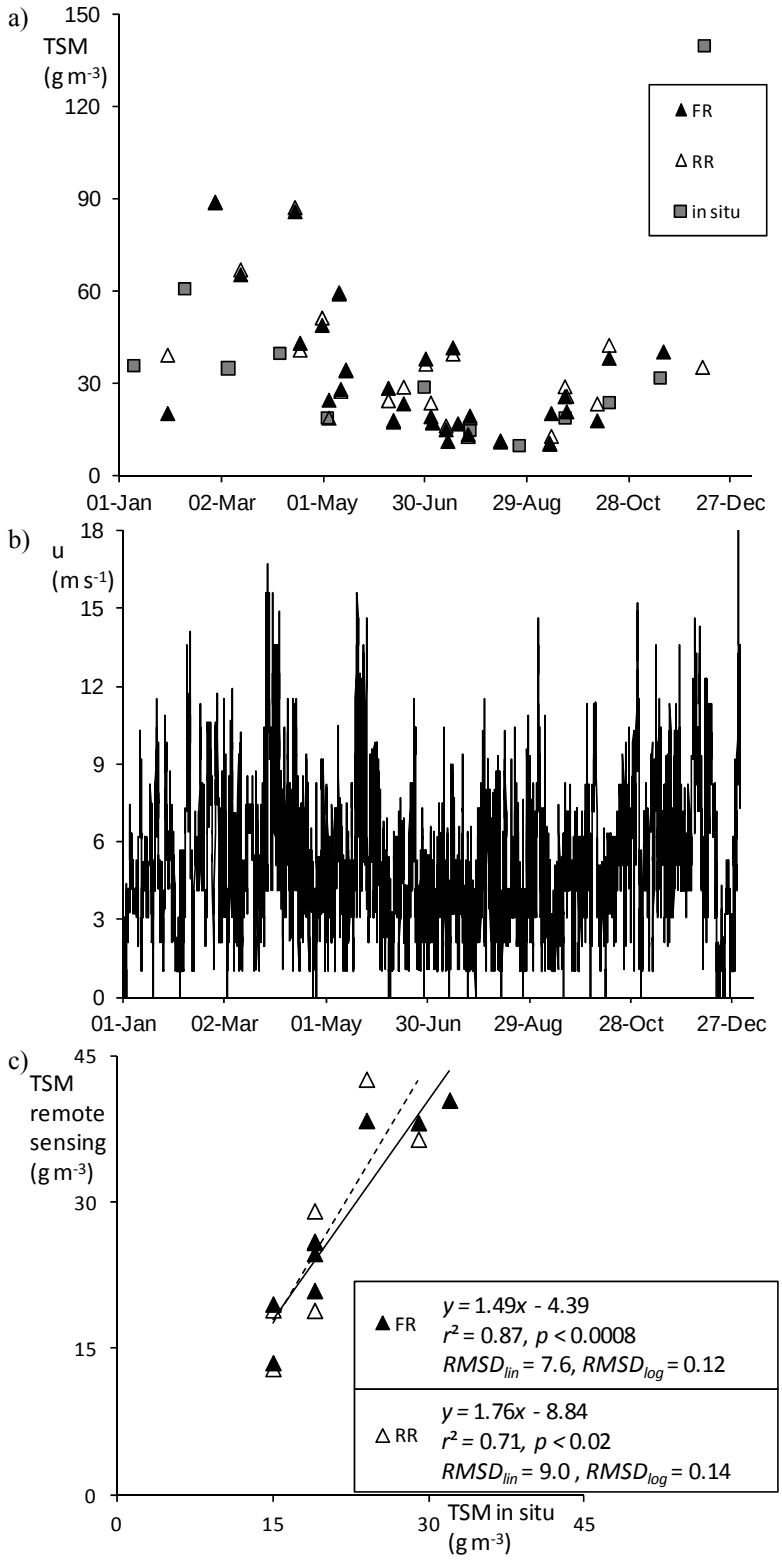

Figure 2. TSM (g m^{-3}) derived from MERIS-FR, from MERIS-RR, and independent in situ measurements of TSM at Markermeer midden, plotted as (a) time series plots complemented by (b) wind speed at Schiphol, and (c) regression for match-ups plus or minus 2 days. FR is shown as a solid line, RR dashed. One outlier was removed from 2c (see text). Root mean square difference (RMSD) is following *Mélin et al.* [2007].

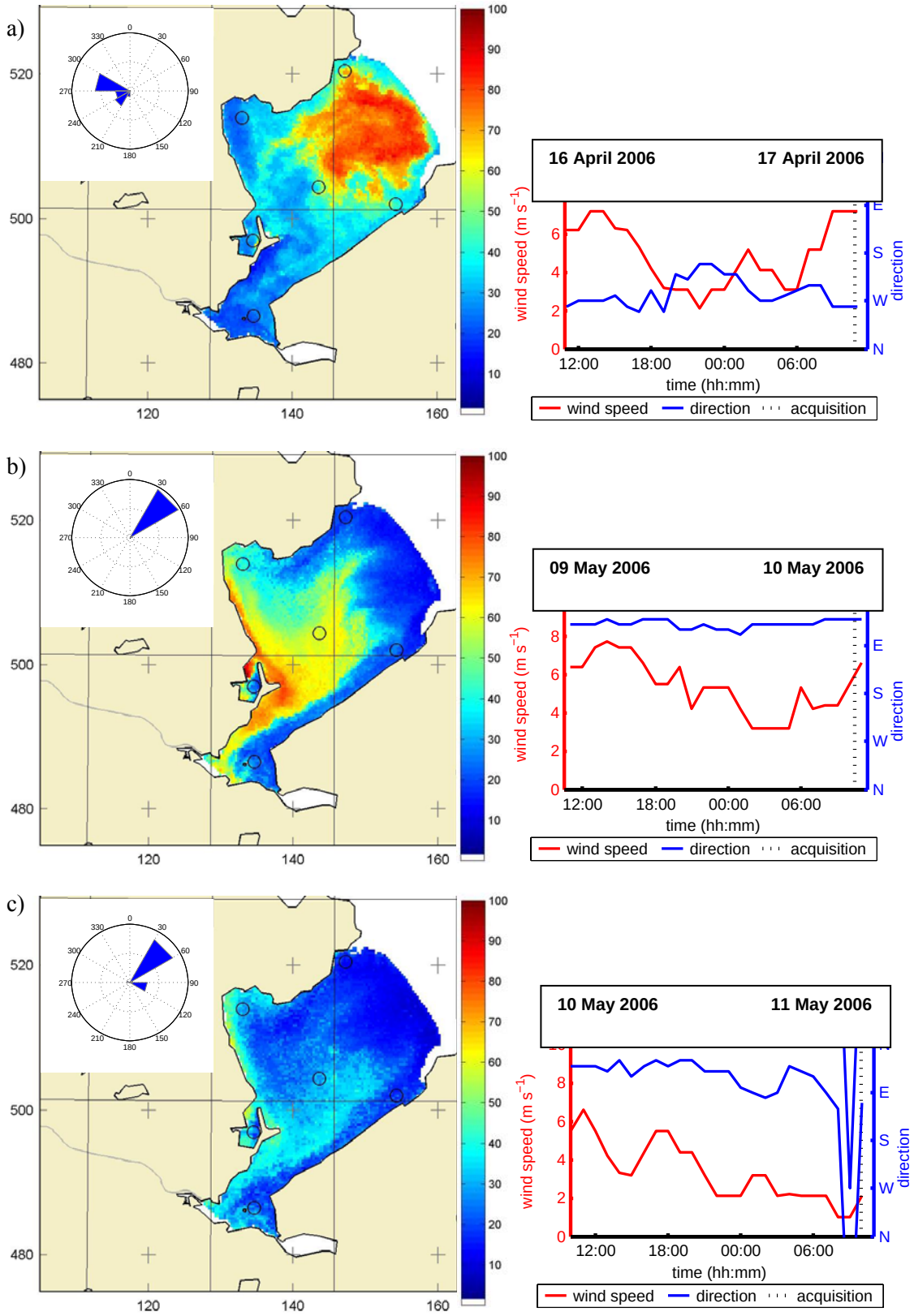
a)
b)
c)
16 April 2006
17 April 2006
09 May 2006
10 May 2006
10 May 2006
11 May 2006
wind speed (m s^{-1})
direction
time (hh:mm)
12:00
18:00
00:00
06:00
wind speed
direction
acquisition
N
E
S
W

Figure 3. TSM concentrations (in g m^{-3}) for different wind directions and speeds. On (a) 17 April high surface concentrations occur in the northeast under the influence of westerly winds. A clear directional TSM signal on (b) 10 May resulting from north-easterly winds is followed by lower concentrations on (c) 11 May caused by settling when the wind is abating. Graphs show wind speed and direction at station Schiphol up to 24 hours prior to satellite data acquisition (indicated by the vertical dotted line). Wind roses show frequency distributions of wind direction in 30° class intervals.

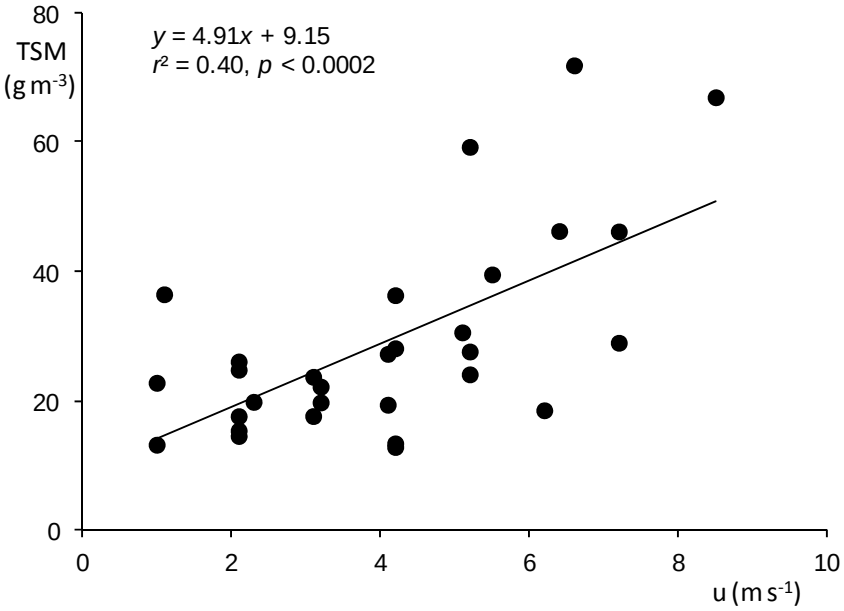

Figure 4. Lake averaged TSM (g m^{-3}) regressed against concurrent hourly wind speed u (m s^{-1}).

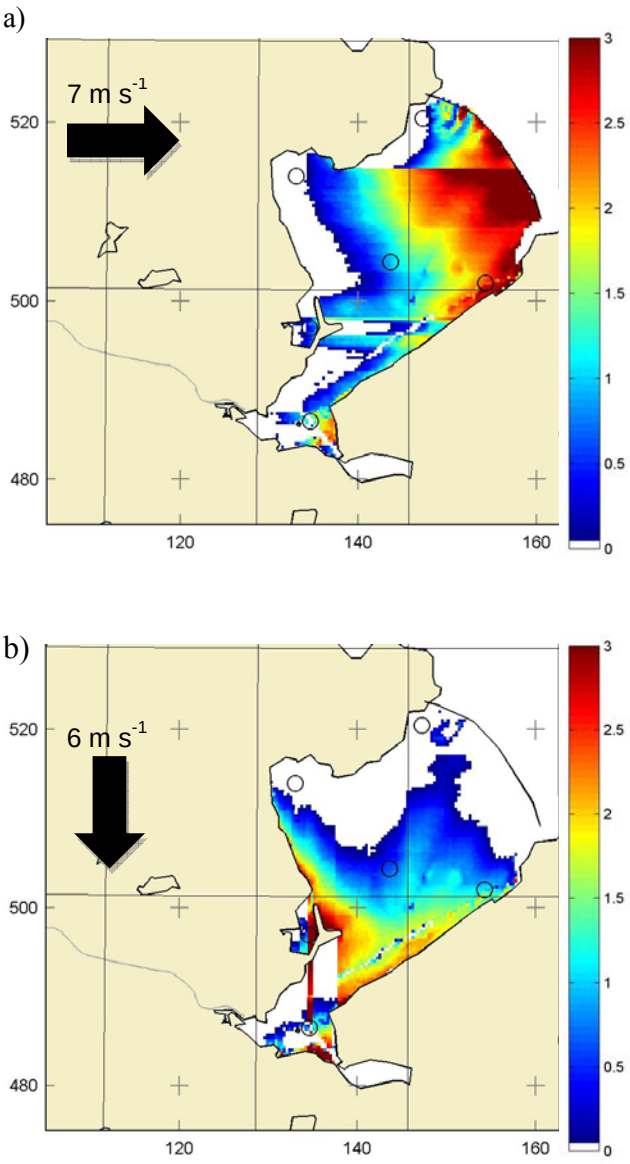

Figure 5. Lakebed area predicted to resuspend at acquisition (cf. Figure 3) on (a) 17 April (measured wind speed 7.2 m s^{-1}, direction 280º) model results for speed 7 direction W; (b) 10 May (measured wind speed 5.5 m s^{-1}, direction 40º) model results for speed 6 direction N. On 11 May wind had abated to 2.1 m s^{-1} with negligible resuspension. White areas are undisturbed by wind. Colored areas indicate predicted resuspension. Color scaling reflects resuspension intensity as indicator of wind energy impacting the bottom.

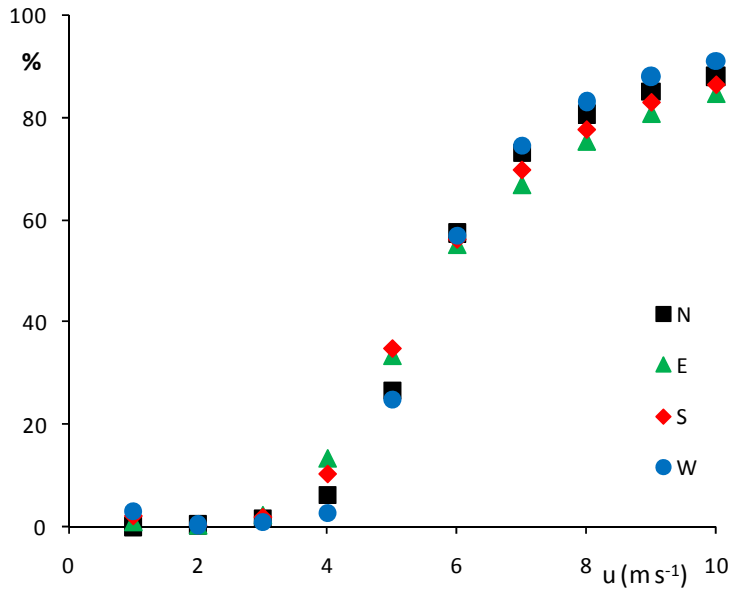

Figure 6. Predicted percentage lakebed area perturbed by wave activity from main wind directions.

Auxiliary Material for Paper 2011WR011121

Wind-induced resuspension in a shallow lake from Medium Resolution Imaging Spectrometer (MERIS) full-resolution reflectances

Marieke A. Eleveld

Vrije Universiteit Amsterdam, Institute for Environmental Studies (VU-IVM), De Boelelaan 1087, 1081 HV Amsterdam, the Netherlands

Eleveld, M. A. (2012) Wind-induced resuspension in a shallow lake from Medium Resolution Imaging Spectrometer (MERIS) full-resolution reflectances, Water Resour. Res., 48(4), W04508, doi:10.1029/2011WR011121.

Introduction

Auxiliary material for this article contains three complementary figures to illustrate the correlation between in situ field measurements and total suspended matter (TSM) derived from remote sensing with the HYDROPT algorithm. These figures serve as additional verification of the results of the HYDROPT algorithm for Markermeer.

This Supporting Auxiliary Material is based on Level2 MERIS Reduced Resolution (MERIS-RR) data (MEGS 7.4 / IPF 5.05) and in situ turbidity (in NTU) from detection of a side-scattering infra-red signal. The signal is produced by an 830 – 890 nm light emitting diode (LED) at an angle of 90 degrees with the detector on an YSI (inc.) 6-Series multiparameter water quality sonde.

Lately, several experiments have been with sensors on measurement poles. They are removed in winter. Two of these sondes have been collecting data at 1 m below the water surface (YSI2) and 1 m above the bottom (YSI1) on measurement station FL42, located 1 km to the southwest of station Markermeer midden (see paper) from March - Nov 2010. The data were kindly made available by Rijkswaterstaat, Ministry of Infrastructure and the Environment (Directie IJsselmeergebied).

The MERIS data were processed to TSM concentrations (g /m3) with the HYDROPT algorithm (see paper), and TSM values at FL42 were saved for plotting.

First, all data were plotted over time. Then, turbidity measurements within a time window of plus or minus 60 mins around image acquisition were selected. Average in situ turbidity was plotted against satellite derived TSM.

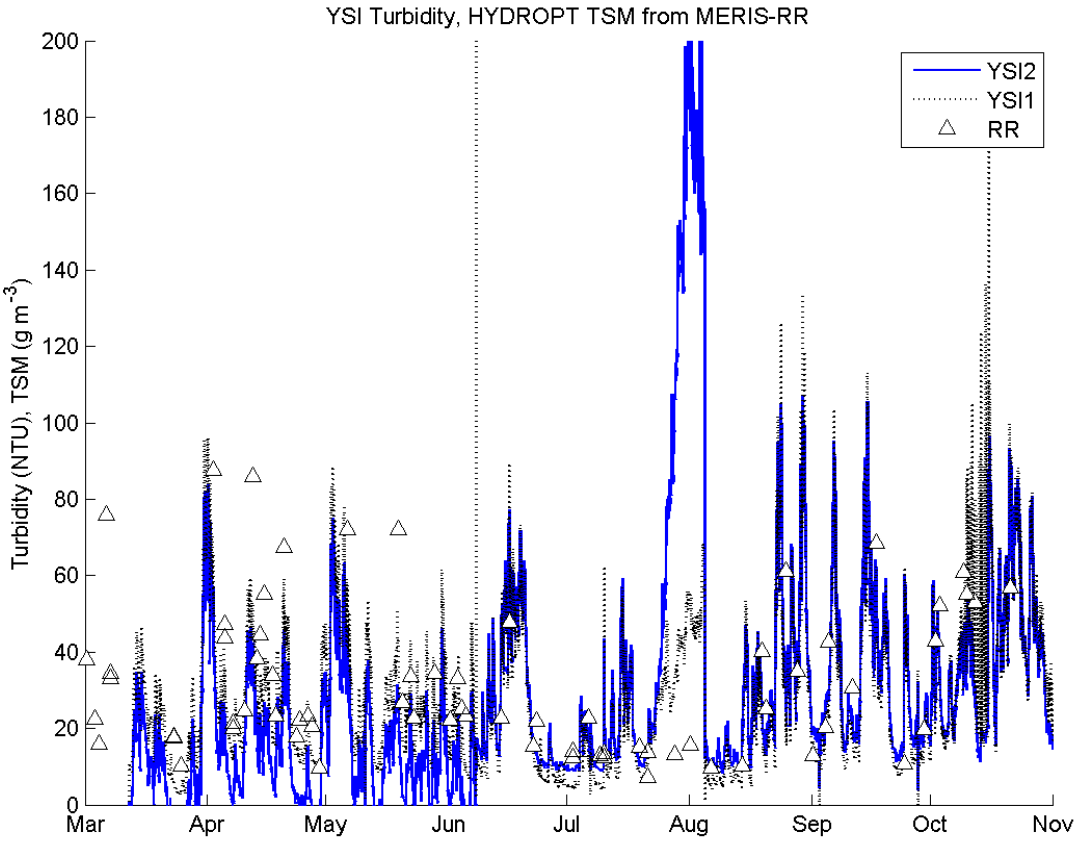

1. 2011wr011121-fs01.tif: TSM (g/m3) derived from MERIS-RR, and independent in situ turbidity measurements plotted as a time series.

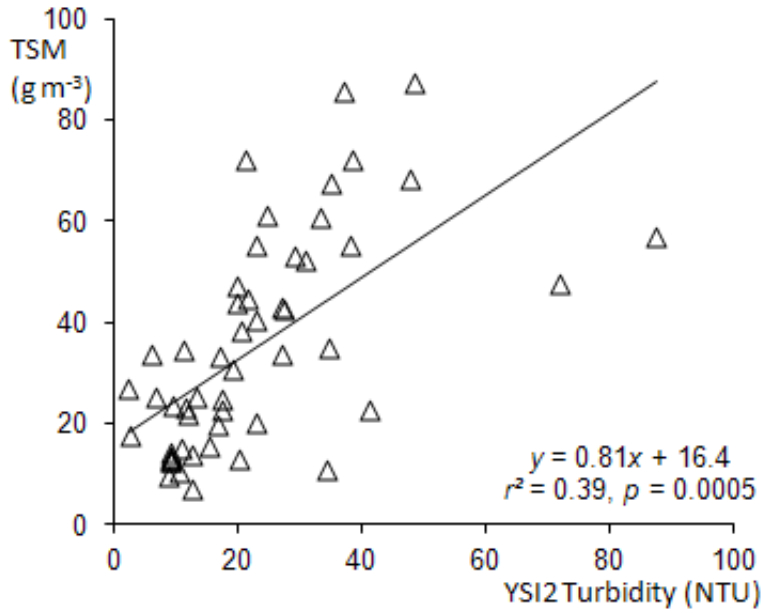

2. 2011wr011121-fs02.tif:In situ turbidity measurements (NTU) versus HYDROPT TSM (g/m3) from MERIS-RR. YSI2 data were collected at 1 m below the water surface. Here, negative YSI2 turbidity values (undershoot) and the peak at the beginning of August (overshoot) were excluded from the regression.

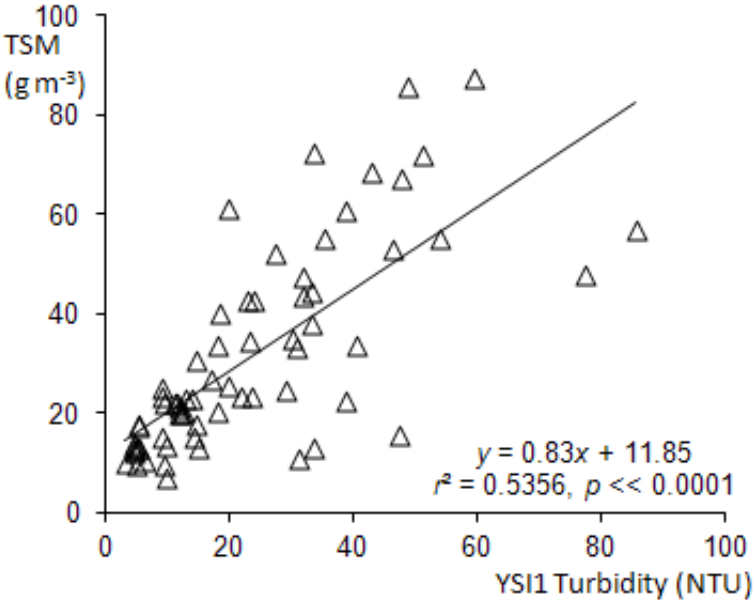

3. 2011wr011121-fs03.tif:Near bottom in situ turbidity measurements (NTU) versus HYDROPT TSM (g/m3) from MERIS-RR.